Design of Electrically Excited Synchronous Machines to Achieve Unity Power Factor in Field Weakening for Long-Haul Electric Trucks

N.B. When citing this work, cite the original published paper.

(article starts on next page)

Design of Electrically Excited Synchronous Machines to Achieve Unity Power Factor in Field Weakening for Long-Haul Electric Trucks

Junfei Tang, *Student Member, IEEE*, and Yujing Liu, *Senior Member, IEEE*

Abstract – **Electrically excited synchronous machines are a promising candidate for long-haul electric trucks due to excellent capability in field weakening. This study aims at concluding a structural design process of the machine for long-haul electric trucks. A criterion of machine design to achieve unity power factor in field-weakening is derived. With this criterion, a minimum level of field current is decided in the design process. Parametric sweeps are applied to decide the optimum slot geometries for stator and rotor. The optimization of slot geometries is multi-objective. In this study, it is to maximize the peak torque while minimize iron-core losses simultaneously. Pareto frontier is used to identify the optimum solutions. The performance of the finalized design is then evaluated. The high-efficiency area is located at high-speed low-torque region which is preferable for long-haul electric trucks. Balance is achieved between copper and iron-core losses during steady-speed intervals of the test cycles which leads to minimum losses in total.**

Index Terms—**Machine design, electric vehicles, electrically excited synchronous machines, optimization.**

I. INTRODUCTION

Electric vehicles (EVs) are a fast-growing area worldwide due to concerns of climate change [1]. Electric machines are key components in the propulsion systems of EVs. Among different types of electric machines for vehicles, permanent magnet synchronous machines (PMSMs) are a prevalent choice. Equipped with rare-earth magnets in the rotor, high torque density can be achieved [2]. However, rare-earth magnets are expensive and are not environmentally friendly in the extraction and refinement process [3]. Moreover, the recycling process of rare-earth materials is still complicated and immature [4]. Comparably in electrically excited synchronous machines (EESMs), a field winding is employed in the rotor with zero consumption of rare-earth materials. In addition, by adjusting the excitation current, the field becomes controllable [5]. Consequently, high starting torque and wide field weakening range can be achieved [6].

Studies on EESM design for vehicles have been pursued. The study presented in [7] covers the design of the entire EESM drives, including machine and brushless excitation system. In machine design, rotor shapes with different curvatures in the pole are studied. Magnetic barriers are introduced to enlarge saliency. In study [8], the local saturation of rotor iron-core of EESM is analyzed. A solution to ease the local saturation by adding magnets on the top of the rotor slot is proposed. The rotor pole shoe arc ratio is also

tuned to keep balance of output torque and THD of back-EMF. In [9], attentions are paid to reduce torque ripples. Three parameters are considered in the optimization process, the tip radii of the upper and lower tooth tip as well as the width of the slot opening. As a result, the torque ripple requirement is achieved.

The previous studies are comprehensive. However, there are some interesting topics not covered in EESM design yet. These are summarized as follows.

- One major advantage of EESMs in vehicle applications is the excellent capability of field weakening at high speed. High efficiency in field weakening is exactly what long-haul electric trucks need. Running on express ways for long time, higher efficiency in field weakening leads to lower battery consumption and consequently longer distance of transportation. Hence EESMs are a promising choice for long-haul electric trucks. However, studies regarding this are quite limited.
- The flexibility of field excitation indicates a controllable power factor. However, whether unity power factor can be achieved from a certain machine design is not concluded yet. This is essential in vehicles since a higher power factor means lower stator current and consequently lower copper losses in stator windings as well as lower losses in inverter switches. Hence high power factor, especially unity power factor, indicates an improvement of performance not only in the electric machine but also in the entire driving system.
- Electric machine designs are multi-objective optimization problems. Specifically, for long-haul electric trucks, both high torque output capability during start-up and low losses in field weakening at high speed are demanded. To tackle this multi-objective optimization problem, a structural design process is needed.
- The test cycles for vehicles used in most studies are worldwide harmonized light-duty vehicles test cycles (WLTC). However, WLTC are only for light-duty vehicles, while for electric trucks, to use test cycles defined specially for heavy-duty vehicles is of interest.

Therefore, the aim of this study is to conclude a structural design process of EESMs for long-haul electric trucks. The machine is expected to achieve unity power factor in field weakening at high speed. To realize this, a criterion of minimum field current is derived. A method to tackle multi-objective optimization to achieve high starting torque and low losses is introduced. In the end, the performance of the machine is evaluated at critical operation points, in the entire operation area of torque-speed map and in test cycles for heavy-duty vehicles.

Junfei Tang is with Electric Power Engineering, Chalmers University of Technology, Gothenburg, Sweden (e-mail: junfei.tang@chalmers.se).

Yujing Liu is with Electric Power Engineering, Chalmers University of Technology, Gothenburg, Sweden (e-mail: yujing.liu@chalmers.se).

II. Machine Modeling and Design Criteria

In this chapter, the machine is modeled in dq-frame. Then the design criterion to achieve unity power factor along high speed envelop in field weakening is concluded.

A. Machine Model

Non-linear electromagnetic properties of iron-cores are considered in the modeling approach here which can be further implemented in finite element method (FEM) analysis. Iron-core losses are taken into account when evaluating different geometrical designs of the machine, but the additional current consumed by iron-core losses is neglected at the machine terminal in the modeling for simplicity.

The electrical characteristics of EESMs can be described as

$$u = Ri + \omega\psi + \frac{d\psi}{dt} \qquad (1)$$

where u, i and ψ are the vectors of voltages, currents and flux linkages in d-axis, q-axis and field

$$u = \begin{bmatrix} u_d \\ u_q \\ u_f \end{bmatrix} \quad , \quad i = \begin{bmatrix} i_d \\ i_q \\ i_f \end{bmatrix} \quad , \quad \psi = \begin{bmatrix} \psi_d \\ \psi_q \\ \psi_f \end{bmatrix} \qquad (2)$$

R and ω are the matrices of resistances and speed

$$R = \begin{bmatrix} R_s & 0 & 0 \\ 0 & R_s & 0 \\ 0 & 0 & R_f \end{bmatrix} \quad , \quad \omega = \begin{bmatrix} 0 & -\omega_r & 0 \\ \omega_r & 0 & 0 \\ 0 & 0 & 0 \end{bmatrix} \qquad (3)$$

The derivatives of flux linkages can be further described by derivatives of currents

$$\frac{d\psi}{dt} = l\frac{di}{dt} \qquad (4)$$

where l is the matrix of incremental inductances

$$l = \begin{bmatrix} l_{dd} & l_{dq} & l_{df} \\ l_{qd} & l_{qq} & l_{qf} \\ l_{fd} & l_{fq} & l_{ff} \end{bmatrix} = \begin{bmatrix} \frac{\partial\psi_d}{\partial i_d} & \frac{\partial\psi_d}{\partial i_q} & \frac{\partial\psi_d}{\partial i_f} \\ \frac{\partial\psi_q}{\partial i_d} & \frac{\partial\psi_q}{\partial i_q} & \frac{\partial\psi_q}{\partial i_f} \\ \frac{\partial\psi_f}{\partial i_d} & \frac{\partial\psi_f}{\partial i_q} & \frac{\partial\psi_f}{\partial i_f} \end{bmatrix} \qquad (5)$$

Then apparent inductances can be defined as

$$L = \begin{bmatrix} L_{dd} & L_{dq} & L_{df} \\ L_{qd} & L_{qq} & L_{qf} \\ L_{fd} & L_{fq} & L_{ff} \end{bmatrix} = \int l\,di \qquad (6)$$

In steady state, the derivatives of flux linkages and currents in dq-frame are zero. The electromagnetic power P and reactive power Q can be calculated as

$$P = 3/2 \cdot \omega_r \cdot (\psi_d \cdot i_q - \psi_q \cdot i_d) = 3/2 \cdot \omega_r \cdot i^T K_P i \qquad (7)$$
$$Q = 3/2 \cdot \omega_r \cdot (\psi_d \cdot i_d + \psi_q \cdot i_q) = 3/2 \cdot \omega_r \cdot i^T K_Q i \qquad (8)$$

where K_P and K_Q are symmetrical matrices

$$K_P = \begin{bmatrix} -L_{qd} & (L_{dd} - L_{qq})/2 & -L_{qf}/2 \\ (L_{dd} - L_{qq})/2 & L_{dq} & L_{df}/2 \\ -L_{qf}/2 & L_{df}/2 & 0 \end{bmatrix} \qquad (9)$$

$$K_Q = \begin{bmatrix} L_{dd} & (L_{dq} + L_{qd})/2 & L_{df}/2 \\ (L_{dq} + L_{qd})/2 & L_{qq} & L_{qf}/2 \\ L_{df}/2 & L_{qf}/2 & 0 \end{bmatrix} \qquad (10)$$

The electromagnetic torque can be formulated as

$$T_{em} = \frac{3}{2} \cdot p \cdot (\psi_d \cdot i_q - \psi_q \cdot i_d) = \frac{3}{2} \cdot p \cdot i^T K_P i \qquad (11)$$

where p is the number of pole pairs.

B. To Achieve Unity Power Factor at High Speed Envelop

From the machine model, the torque-speed envelop can be described, where the maximum torque generated by the machine at each speed is indicated. In heavy-duty applications, the vehicle runs on express ways at high speed for long time. Therefore, it is important to achieve high power factor at high speed. This is an advantage of EESMs. By adjusting the field current of an EESM, high power factor, even unity power factor, can be achieved.

The criterion to achieve unity power factor can be derived by setting Q in (8) to zero. For simplicity, mutual inductances between d- and q-axis windings and between q-axis and field windings are neglected. This leads to

$$Q = L_{dd} \cdot i_d^2 + L_{qq} \cdot i_q^2 + L_{df} \cdot i_f \cdot i_d = 0 \qquad (12)$$

The unity power factor can be shown in dq-frame as an ellipse

$$\frac{(i_d + a)^2}{a^2} + \frac{i_q^2}{b^2} = 1 \qquad (13)$$

where the squares of the semi-axes are

$$a^2 = \frac{1}{4} \cdot \frac{L_{df}^2}{L_{dd}^2} \cdot i_f^2 \quad and \quad b^2 = \frac{1}{4} \cdot \frac{L_{df}^2}{L_{dd} \cdot L_{qq}} \cdot i_f^2 \qquad (14)$$

Furthermore, at high speed, the machine operates in field weakening. This means that the machine is working at the intersection between current limit circle and voltage limit ellipse. To guarantee unity power factor in this situation, the unity power factor ellipse needs to come across this intersection as well. To make sure that a solution in this situation is available, the center of the unity power factor ellipse described in (13) must locate outside of the current limit circle. This criterion can be formulated as

$$I_{s.max} < \frac{L_{df}}{L_{dd}} \cdot I_{f.max} \qquad (15)$$

The inductances L_{df} and L_{dd} can be further formulated as

$$L_{df} = \frac{N_d \cdot N_f}{\Re_m} \cdot \frac{N_{s.ser}}{N_{f.par}} \qquad L_{dd} = \frac{N_d \cdot N_d}{\Re_d} \cdot \frac{N_{s.ser}}{N_{s.par}} \qquad (16)$$

where N_d is the equivalent number of half-turns per pole in stator d-axis, N_f is the number of turns per pole in field winding, $\Re_m$ is the reluctance of field winding flux path, $\Re_d$ is the d-axis reluctance of stator winding flux path, $N_{s.ser}$ and $N_{s.par}$ are the numbers of series and parallel branches in stator winding respectively, and $N_{f.par}$ is the number of parallel branches in field winding. N_d can be further formulated as

$$N_d = k_w \cdot q \cdot r \cdot N_s \qquad (17)$$

where k_w is the winding factor, q is the number of slots per pole per phase, r is the number of winding layers and N_s is the number of turns per coil in stator winding. Then the criterion (15) can be concluded as

$$I_{f.max} > k_w \cdot q \cdot r \cdot \frac{N_s}{N_f} \cdot \frac{N_{f.par}}{N_{s.par}} \cdot \frac{\Re_m}{\Re_d} \cdot I_{s.max} \qquad (18)$$

In addition, $\Re_d$ equals the mutual reluctance $\Re_m$ in parallel with the leakage reluctance $\Re_\sigma$. Due to the large value of $\Re_\sigma$ compared with $\Re_m$,

$$\Re_d = \Re_m // \Re_\sigma = \frac{\Re_m \cdot \Re_\sigma}{\Re_m + \Re_\sigma} \approx \Re_m \qquad (19)$$

With this approximation, (18) becomes

$$I_{f.max} > k_w \cdot q \cdot r \cdot \frac{N_s}{N_f} \cdot \frac{N_{f.par}}{N_{s.par}} \cdot I_{s.max} \qquad (20)$$

This is the criterion to decide the minimum field current level to guarantee unity power factor in field weakening.

III. Design Specifications and Evaluation Test Cycles

In this chapter, the design specifications of the machine are derived from those of a long-haul truck. Test cycles are introduced to evaluate the overall performance of the machine.

A. Vehicle Model

The long-haul truck considered in this study is described by the parameters listed in TABLE I [10]. Torque requested from the machine to accelerate the truck can be formulated as

$$T_{\text{truck}} = r_{\text{tire}} \cdot \frac{m_{\text{truck}} \cdot a_{\text{truck}} + F_{\text{road}}}{k_{\text{gear}} \cdot \eta_{\text{gear}}} \quad (21)$$

where r_{tire} is the radius of tires, m_{truck} is the weight of the truck, a_{truck} is the acceleration of the truck, and F_{road} is the total resistance which is the sum of air drag F_{air}, rolling resistance F_{roll} and grade force F_{grade}

$$F_{\text{road}} = F_{\text{air}} + F_{\text{roll}} + F_{\text{grade}} \quad (22)$$

These three forces can be formulated as

$$
\begin{aligned}
F_{\text{air}} &= \frac{\rho_{\text{air}} \cdot C_{\text{drag}} \cdot A_{\text{truck}}}{2} \cdot (v_{\text{truck}} - v_{\text{wind}})^2 \\
F_{\text{roll}} &= C_{\text{roll}} \cdot m_{\text{truck}} \cdot g \cdot \cos \alpha_{\text{truck}} \\
F_{\text{grade}} &= m_{\text{truck}} \cdot g \cdot \sin \alpha_{\text{truck}}
\end{aligned}
\quad (23)
$$

where ρ_{air} is the density of air, C_{drag} is the aerodynamic air drag coefficient, A_{truck} is the effective frontal area, v_{truck} is the speed of the truck, v_{wind} is the speed of wind which is considered as zero in this study, C_{roll} is the rolling resistance coefficient, g is the acceleration of gravity, α_{truck} is the angle of climbing slope.

TABLE I
PARAMETERS OF THE LONG-HAUL TRUCK

Parameter	Symbol	Value	Unit
weight	m_{truck}	40 000	kg
maximum vehicle speed		100	km/h
effective frontal area	A_{truck}	$9.7 \cdot 0.86$	m²
aerodynamic drag coefficient	C_{drag}	0.53	
rolling resistance coefficient	C_{roll}	0.0051	
coefficient of friction		0.8	
gear ratio	k_{gear}	19	
gear efficiency	η_{gear}	94	%
number of electric machines		2	
number of tires		12	
tire size		315/70R22.5	

B. Critical Operation Points

As for a long-haul truck, it must be able to operate at three critical points: (1) starting up on a slope of 12%; (2) climbing on slope of 6% at 50 km/h; (3) cruising on flat road at 80 km/h. These critical operation points are shown in TABLE II. Based on the vehicle model and the parameters mentioned in TABLE I, the critical points defined for each machine can be derived from the critical points defined for the vehicle. In addition, since 8000 rev/min is the point that the machine should run for long time, a good efficiency should be achieved there.

TABLE II
CRITICAL OPERATION POINTS DEFINED FOR THE LONG-HAUL TRUCK

Operation	Duration Time [min]	Vehicle Speed [km/h]	Vehicle Slope [%]	Machine Speed [rev/min]	Machine Torque [N·m]
peak torque	5	0 ~ 30	12	3000	800
climbing	20	50	6	5000	350
cruising	long time	80	0	8000	50

C. Mechanical and Electrical Dimensions of the Machine

The machine needs to be dimensioned to fit the space on the truck. The outer diameter and length of the housing are given in TABLE III, based on which the stack length and the outer diameter of laminations are estimated. The electrical dimensions are based on the power needed to drive the truck and the output capacity of the inverters driving the machines.

TABLE III
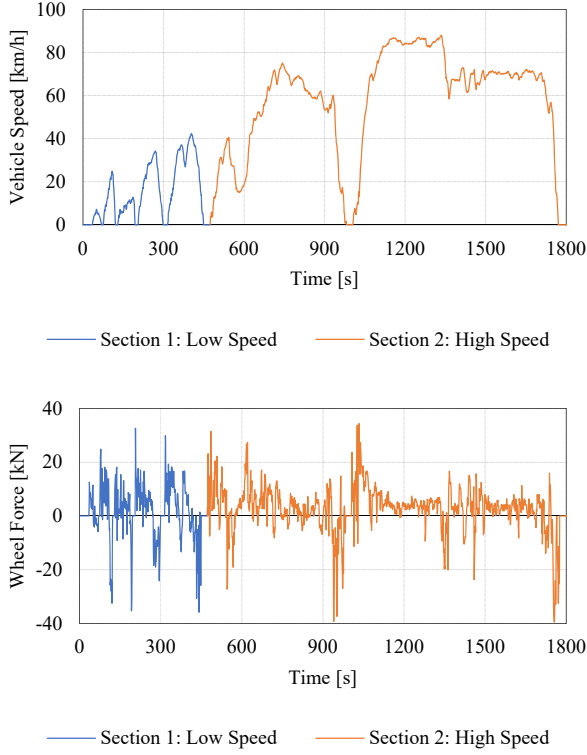MECHANICAL AND ELECTRICAL DIMENSIONS OF THE EESM

| Parameter	Symbol	Value	Unit
outer diameter of housing		300	mm
length of housing		600	mm
outer diameter of lamination	OD_{stator}	270	mm
diameter of Shaft	ID_{rotor}	50	mm
stack length	L_{stack}	360	mm
maximum power	P_{max}	250	kW
nominal dc-link voltage	U_{dc}	800	V
maximum stator voltage amplitude	$U_{\text{s.amp.max}}$	461	V
maximum stator current amplitude	$I_{\text{s.amp.max}}$	450	A

D. Automotive Test Cycles

To evaluate the overall performance of the electric machine in practical activities, a set of automotive test cycles for heavy-duty trucks, CHTC-TT, is introduced in this study. CHTC-TT is one of the scenarios described in the China automotive testing cycles (CATC) [11]. CATC is concluded in 2019 from a research covering over 17 vehicle models, 2.5 million data inputs, 700 thousand car owners and 31 provinces in China. Categorizations of CATC are shown in Fig. 1. The speed curve of CHTC-TT and the derived wheel force based on the vehicle model are shown in Fig. 2 (a). As one step further, the torque-speed points of the machine are derived. These torque-speed points from test cycles and the critical points are placed on the torque-speed map of the machine in Fig. 2 (b). The machine works for most time at high speed but low torque region.

Fig. 1 Categorizations of China automotive test cycles (CATC).

(a) Test cycles for tractor and trailer (CHTC-TT).
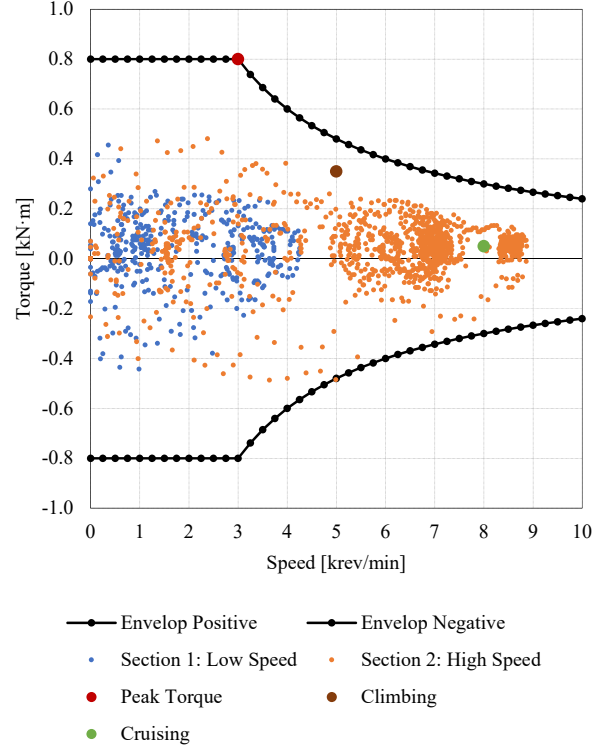
(b) Points derived from CHTC-TT in torque-speed map.

Fig. 2   CHTC-TT and the derived torque-speed points.

IV. MACHINE DESIGN

In this chapter, the machine design process is introduced. Firstly, a commonly used winding arrangement is adopted. Thereafter, the numbers of parallel branches and strands are selected based on the level of stator current. Finally, assisted by parametric sweep in FEM analysis, the number of turns is decided together with airgap diameter and slot geometries.

A. Winding Arrangement

The winding arrangement adopted in this study is 8-pole 48-slot with shot-pitch of 1 slot. Since this is a well-known common winding arrangement, the manufacturing process should be mature which means this choice is practical. The parameters of this arrangement are listed in TABLE IV.

TABLE IV
WINDING ARRANGEMENT

Parameters	Symbol	Value
number of phases	m	3
number of pole pairs	p	4
number of slots per pole per phase	q	2
number of layers	r	2
pole pitch	τ	6
coil pitch	y	5
number of slots	Q	48
winding factor	k_w	0.933

B. Parallel Branches and Strands

From manufacturing perspectives, a strand diameter between 0.7 mm and 1.0 mm would be a practical choice. In this study, the strand diameter is arbitrarily decided as 1.0 mm for both stator and field windings. The cross-section area of each copper strand is therefore

$$A_{\text{strand}} = \pi \cdot r_{\text{strand}}^2 \tag{24}$$

Considering thermal issues, the current densities of stator and field windings are set as 15 and 10 A/mm² respectively.

For the stator winding, the total copper area per phase able to conduct the maximum current can be decided as

$$A_{\text{phase}} = \frac{I_{\text{s.rms.max}}}{J_{\text{s.rms.max}}} \tag{25}$$

This amount of current is shared by several parallel branches

$$A_{\text{branch}} = \frac{A_{\text{phase}}}{N_{\text{branch}}} \tag{26}$$

In each branch, the current is not split any more. The number of strands is therefore decided by taking of ceiling of the ratio

$$N_{\text{strand}} = \text{ceiling}\left\{\frac{A_{\text{branch}}}{A_{\text{strand}}}\right\} \tag{27}$$

For the field winding, the design procedure is the opposite. To guarantee the same amount of MMF generated from each pole, N_{branch} is set to 1. In addition, the field excitation is expected to be contactless through an H-bridge inverter, a rotating transformer and a diode rectifier. Therefore, a higher resistance of the field winding is preferred to minimize the voltage drop across the diodes in percentage. Hence N_{strand} is set to 1. The level of field current is then decided backwards.

C. Airgap and Slot Geometry

The stator and rotor geometries are parameterized as shown in Fig. 3. $Bs0$, $Bs1$ and $Bs2$ mean the widths of slot opening, slot top and slot bottom. $Hs0$, $Hs1$ and $Hs2$ mean the heights of slot opening, slot wedge and slot body. Rs means the fillet radius of slot corner.

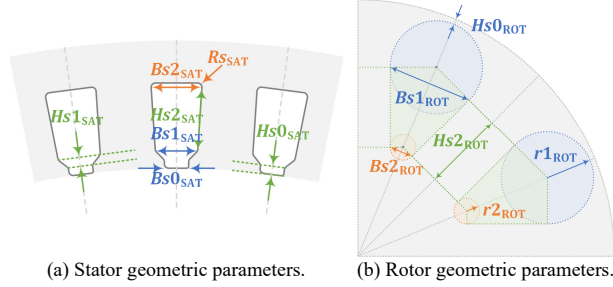(a) Stator geometric parameters.   (b) Rotor geometric parameters.

Fig. 3   Parameters of the stator and rotor geometries.

1) Fixed Parameters

A few parameters are fixed in the analysis of slot geometries as listed in TABLE V. The airgap thickness is set to 1.5 mm to avoid radial collisions. The values of other parameters in the table are believed to be practical choices in terms of manufacturing and would not significantly affect the machine performance. The rotor is decided as closed-slot to prevent the field windings from flying out at high speed.

TABLE V
FIXED GEOMETRICAL PARAMETERS

Parameter	Symbol	Value	Unit
airgap thickness	t_{airgap}	1.5	mm
stator	$Hs0_{\text{STA}}$	1	mm
	$Hs1_{\text{STA}}$	1	mm
	$Bs0_{\text{STA}}$	2	mm
	Rs_{STA}	1	mm
rotor	$Hs0_{\text{ROT}}$	2	mm
	$Hs1_{\text{ROT}}$	0	mm
	$Bs0_{\text{ROT}}$	0	mm

2) Slot Geometries

Parametric sweeps are applied to decide the optimum geometries of stator and rotor slots. The slot width and height are swept while the stator and rotor slot areas are fixed in the sweep. Parallel tooth in stator and parallel pole in rotor are set as constraints as well, which means

$$Bs2_{\text{STA}} = Bs1_{\text{STA}} + 2 \cdot Hs2_{\text{STA}} \cdot \tan \alpha_{\text{STA}} \quad (28)$$
$$Bs2_{\text{ROT}} = Bs1_{\text{ROT}} - 2 \cdot Hs2_{\text{ROT}} \cdot \tan \alpha_{\text{ROT}} \quad (29)$$

where

$$\alpha_{\text{STA}} = \pi/Q \quad , \quad \alpha_{\text{ROT}} = \pi/2/p \quad (30)$$

The stator and rotor slot areas can be formulated as

$$
\begin{aligned}
A_{\text{slot.STA}} = & (Bs1_{\text{STA}} + Bs2_{\text{STA}}) \cdot Hs2_{\text{STA}}/2 \\
& + Rs_{\text{STA}}^2 \cdot (\pi/2 + \alpha_{\text{STA}} + \sin \alpha_{\text{STA}} \cdot \cos \alpha_{\text{STA}}) \\
& + [Rs_{\text{STA}} \cdot (1 + \sin \alpha_{\text{STA}})] \\
& \cdot (Bs2_{\text{STA}} - 2 \cdot Rs_{\text{STA}} \cdot \cos \alpha_{\text{STA}})
\end{aligned}
\quad (31)
$$

$$
\begin{aligned}
A_{\text{slot.ROT}} = & (r1_{\text{ROT}} + r2_{\text{ROT}})/\cos \alpha_{\text{ROT}} \cdot Hs2_{\text{ROT}} \\
& + r1_{\text{ROT}}^2 \cdot (\pi - \beta_{\text{ROT}}) + r2_{\text{ROT}}^2 \cdot \beta_{\text{ROT}}
\end{aligned}
\quad (32)
$$

where

$$\beta_{\text{STA}} = \pi/2 - \alpha_{\text{STA}} \quad , \quad \beta_{\text{ROT}} = \pi/2 - \alpha_{\text{ROT}} \quad (33)$$
$$r1_{\text{ROT}} = \frac{Bs1_{\text{ROT}}}{2 \cdot \cos \alpha_{\text{ROT}}} \quad , \quad r2_{\text{ROT}} = \frac{Bs2_{\text{ROT}}}{2 \cdot \cos \alpha_{\text{ROT}}} \quad (34)$$

V. RESULTS

In this chapter, the results of the parametric sweep analysis are firstly presented to finalize the design. Then the flux distributions of the machine at no load and peak torque are presented. In the end, the machine performances are evaluated at critical points, in efficiency map and in test cycles.

A. Results of Parametric Sweeps

Parametric sweeps are applied in optimization to maximize the peak torque while minimize losses. As mentioned before, the air gap diameter, widths and heights of slots are varied while the slot areas are kept constant. The maximum torque versus core-loss of each geometrical design is presented in Fig. 4. The copper losses are almost the same for all cases and therefore are not presented here. The geometries with the same air gap diameter are illustrated in the same color. The optimum points are expected to achieve high torque and low iron-core losses at the same time. The Pareto frontier regarding this target is illustrated in the graph. Additionally, there are only three candidates lay above 800 N·m. The differences of torque level between them are minor. Therefore, it is clear to select the one with the lowest core-loss among the three, which is marked by a circle in blue. The parameters of this finalized design are listed in TABLE VI and TABLE VII.
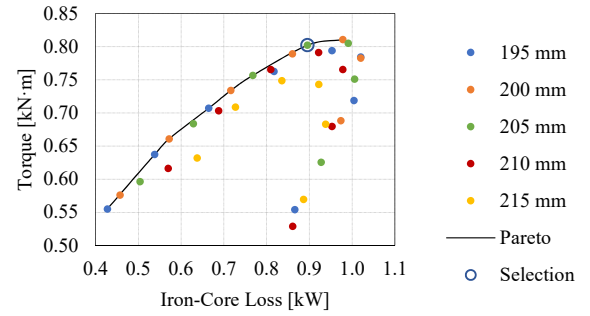

Fig. 4   Peak torque versus iron-core losses of different geometries.

TABLE VI
WINDING AND GEOMETRICAL PARAMETERS OF THE FINALIZED DESIGN

Parameter	Stator		Rotor	
	Value	Unit	Value	Unit
d_{airgap}	205	mm	205	mm
N_{branch}	4		1	
N_{coil}	2		8	
N_{turn}	5		270	
N_{strand}	7		1	
$Hs2$	14.58	mm	26.62	mm
$Bs1$	7.79	mm	28.99	mm
$Bs2$	9.70	mm	6.94	mm

TABLE VII
ELECTRICAL PARAMETERS OF THE FINALIZED DESIGN

Parameter	Symbol	Value	Unit
stator resistance @ 100°C	R_s	19.55	mΩ
field resistance @ 100°C	R_f	54.71	Ω
d-axis self-inductance @ zero current	L_{dd}	1.30	mH
q-axis self-inductance @ zero current	l_{qq}	1.30	mH
field self-inductance @ zero current	l_{ff}	20.29	H
mutual inductance @ zero current	l_{df}	92.80	mH

B. Flux Distributions

The flux distributions of the machine with the finalized geometry at no load and peak torque are presented in Fig. 5. The maximum field current of 7.854 A is applied in both cases. The peak torque is achieved with the maximum stator current amplitude of 450 A and a current angle of 107°.

At no load, the teeth and yoke of the stator are evenly saturated. Comparably, at peak torque, some of the stator teeth become more saturated due to armature reaction. This leads to a reverse of saliency from $L_{dd} > L_{qq}$ to $L_{dd} < L_{qq}$. Consequently, the peak torque is achieved at a current angle of 107° instead of being at first quadrant in dq-frame.

In addition, the saturation of rotor pole is eased at peak torque due to the amount of negative d-axis current applied from the stator winding. The flux generated from the negative d-axis current counteracts the flux generated from the field winding and eases the saturation in rotor pole body. Moreover, the saturation of the rotor pole shoes becomes uneven. This is due to the q-axis current applied from the stator winding. The flux generated from the q-axis current cancels the flux at one tip of the pole shoe while enhances the flux at the other tip.
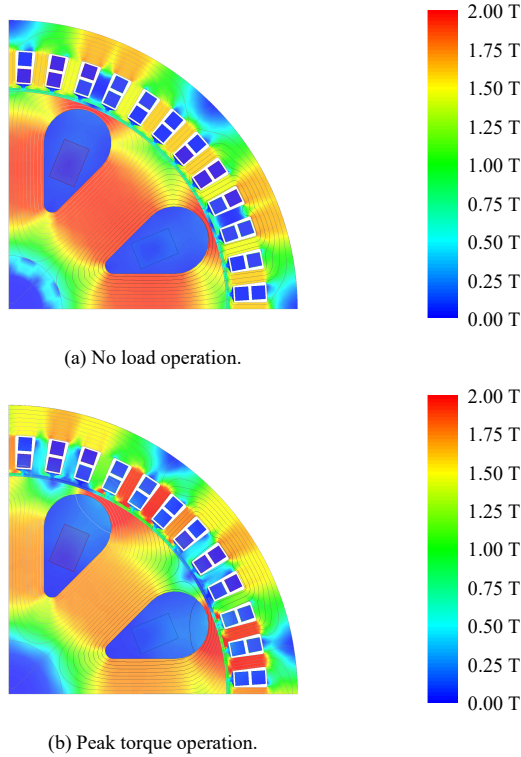

(a) No load operation.

(b) Peak torque operation.

Fig. 5   Flux density distribution.

C. Verification of Critical Points

Flux linkage maps are generated by varying d-axis, q-axis and field currents in FEM parametric sweeps. Then the solutions of d-axis, q-axis and field currents at any specific torque-speed point can be obtained through iterations to minimize copper and iron-core losses. The solutions of the critical points are then verified in FEM. The results from iterations agree to the FEM results as shown in TABLE VIII.

TABLE VIII
VERIFICATION OF CRITICAL OPERATION POINTS OF THE LONG-HAUL TRUCK

		Peak Torque	Climbing	Cruising	Unit
Speed		3000	5000	8000	rev/min
Torque	Iteration	802.07	350.00	50.00	N·m
	FEM	802.02	350.46	50.14	
Power	Iteration	251.98	183.26	41.89	kW
	FEM	251.96	183.50	42.00	
η	Iteration	96.11	97.70	97.82	%
	FEM	96.11	97.70	97.92	
$\cos\varphi$	Iteration	0.93	0.98	0.93	
	FEM	0.90	0.97	0.93	
P_{Cu}		9.31	3.19	0.34	kW
P_{Fe}	Iteration	0.90	1.13	0.59	kW
	FEM	0.90	1.14	0.55	

D. Efficiency Map

The efficiency map of the machine can be achieved by extending the usage of the iteration algorithm to all points in the torque-speed map. Only copper and iron-core losses are considered in the efficiency calculation. The sum of copper and iron-core losses is set as the target for minimization in the iteration algorithm. Results are presented in Fig. 6. The envelop at high speed is steadily at approximately 300 kW. This is due to the ability of the machine to keep unity power factor at high speed. This ability is achieved by following the field current criterion introduced in (20). The high efficiency area is successfully set at high speed but low torque region, which is the mostly used condition as described in Fig. 2 (b).
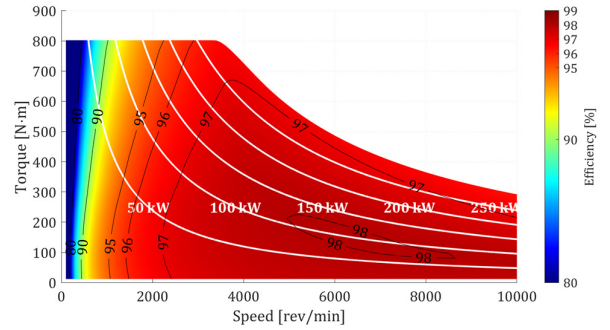

Fig. 6   Efficiency map of the machine at torque-speed coordinates considering only copper losses and iron losses.

E. Performance in Test Cycles

The machine performance is evaluated in CHTC-TT. The results are presented in Fig. 7. The difference between input and output power are minor. This is due to that, in CHTC-TT the truck mostly runs at high speed but low torque, which fits exactly the high efficiency area in Fig. 6. The copper losses are generally higher than iron-core losses during acceleration and deceleration when high level of torque is demanded. In contrast, when the vehicle runs steadily at almost constant speed, the torque demand is low and the copper losses are at a similar level of iron-core losses. Balance of the two is a well-known rule of thumb to achieve high efficiency of machine design, and this is how good efficiency is achieved here.
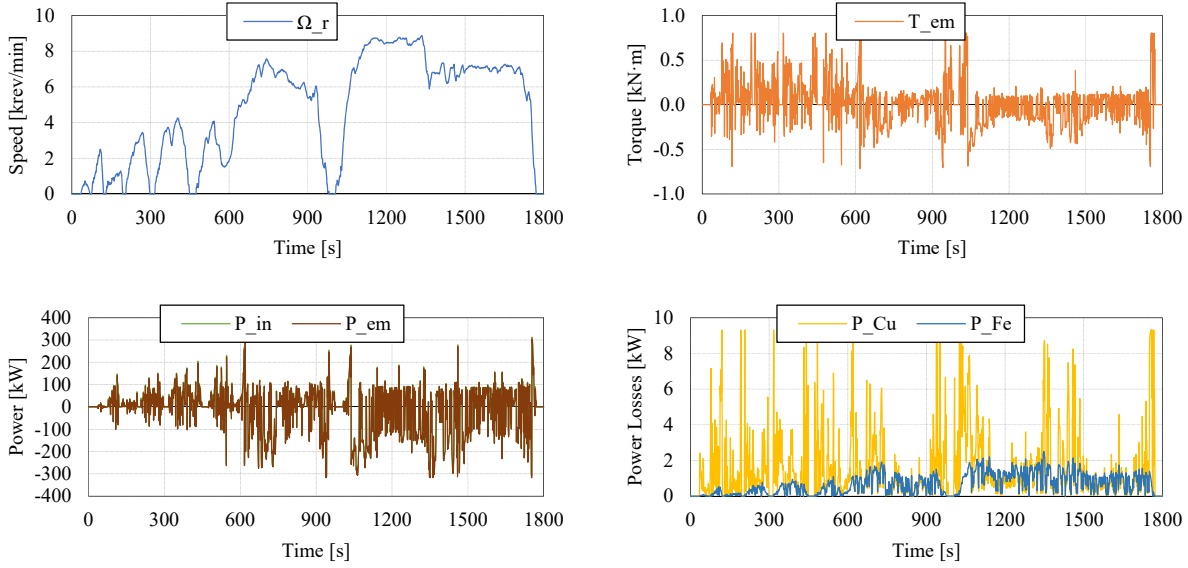
Fig. 7   Machine performance evaluated in CHTC-TT.

VI.   Conclusions

In this study, a structural design process of electrically excited synchronous machines for long-haul electric trucks is concluded. The machine design is guided by a criterion showing the minimum field current level. With this criterion applied, unity power factor can be achieved along the torque-speed envelop of the machine at high speed. Parametric sweeps are applied to optimize the slot geometries of stator and rotor. The parametric study is to select a geometry with which high peak torque and low core-losses are achieved at the same time. In the end, the performance of the machine is evaluated. The high-efficiency area of the machine is located at high-speed low-torque region which is preferable in long-haul electric truck applications. Balance between copper losses and iron-core losses is achieved during steady-speed intervals of the test cycles. This leads to minimum losses in total. As the future work, a 'virtual' type of the machine will be tested with the assistance of an emulator. The machine will be prototyped in the end and tested practically.

VII.   References

[1]   International Energy Agency, "Global EV Outlook 2019," International Energy Agency, 2019.

[2]   J. D. Widmer, R. Martin and M. Kimiabeigi, "Electric Vehicle Traction Motors without Rare Earth Magnets," *Sustainable Materials and Technologies,* vol. 3, pp. 7-13, 2015.

[3]   D. G. Dorrell, A. M. Knight, M. Popescu, L. Evans and D. A. Staton, "Comparison of Different Motor Design Drives for Hybrid Electric Vehicles," in *2010 IEEE Energy Conversion Congress and Exposition*, Atlanta, 2010.

[4]   Y. Yang, A. Walton, R. Sheridan, K. Güth, R. Gauß, O. Gutfleisch, M. Buchert, B.-M. Steenari, T. V. Gerven, P. T. Jones and K. Binnemans, "REE Recovery from End-of-Life NdFeB Permanent MagnetScrap: A Critical Review," *Journal of Sustainable Metallurgy,* vol. 3, no. 1, pp. 3 - 30, 2017.

[5]   J. Tang and Y. Liu, "Design and Experimental Verification of a 48 V 20 kW Electrically Excited Synchronous Machine for Mild Hybrid Vehicles," in *2018 XIII International Conference on Electrical Machines (ICEM)*, Alexandroupoli, 2018.

[6]   J. Tang and Y. Liu, "Comparison of Copper Loss Minimization and Field Current Minimization for Electrically Excited Synchronous Motor in Mild Hybrid Drives," in *19th European Conference on Power Electronics and Applications (EPE'17 ECCE Europe)*, Warsaw, Poland, 2017.

[7]   E. M. Illiano, "Design of a Highly Efficient Brushless Current Excited Synchronouos Motor for Automotive Purposes," Swiss Federal Institute of Technology in Zurich (ETH Zurich), Zurich, 2014.

[8]   L. Huang, Z. Zhu and W. Chu, "Optimization of Electrically Excited Synchronous Machine for Electrical Vehicle Applications," in *Machines and Drives (PEMD 2016), 8th IET International Conference on Power Electronics*, Glasgow, UK, 2016.

[9]   C. Stancu, T. Ward, K. M. Rahman, R. Dawsey and P. Savagian, "Separately Excited Synchronous Motor With Rotary Transformer for Hybrid Vehicle Application," *IEEE Transactions on Industry Applications,* vol. 54, no. 1, pp. 223-232, 2018.

[10]   H. Stenvall, "Driving Resistance Analysis of Long Haulage Trucks at Volvo," Chalmers University of Technology, Applied Mechanics, Gothenburg, 2010.

[11]   Standardization Administration of P.R.C, GB/T 38146.2-2019 China Automotive Test Cycle Part 2: Heavy-Duty Vehicle, Standardization Administration of P.R.C, 2019.

VIII.   Biographies

Junfei Tang (S'16) received B.Eng. in electrical engineering from Jiangsu University, Zhenjiang, China, in 2013, and M.Sc. in electric power engineering from Chalmers University of Technology, Gothenburg, Sweden, in 2016. Now he is pursuing his doctoral study in electric machines and power electronics in Chalmers University of Technology.

Yujing Liu (SM'12) received B.Sc., M.Sc. and Ph.D. degrees in electrical engineering from Harbin Institute of Technology, Harbin, China, in 1982, 1985, and 1988, respectively. In 1996-2013, he worked in ABB Corporate Research, Västerås, Sweden. Since 2013, he is a professor on electrical power engineering in Chalmers University of Technology, Gothenburg, Sweden. Yujing Liu is a senior IEEE member and a member in Swedish Standard Committee on Electrical Machines.